scientific reports

Check for updates

OPEN

Meta-lens-based circularly polarized fixed-beam antenna for high-gain wideband millimeter-wave applications

Ubaid Ullah[1]✉, Slawomir Koziel[2,3] & Anna Pietrenko-Dabrowska[3]

A planar metamaterial lens-based single-element circularly polarized (CP) antenna for millimeter wave (mm-wave) band applications is presented. The proposed antenna consists of a modified patch excited by a single-point-fed coaxial probe and two displaced layers of a novel meta-lens design. The modified structure allows for the simultaneous excitation of orthogonal components with equal magnitudes. To realize the gain enhancement of the proposed design, a novel meta-lens is designed based on meta-atoms of subwavelength size arranged in a disconnected cross-shape repeated pattern. To effectively focus the outgoing CP wave radiated by the antenna, the focal distance is meticulously optimized. Two layers of the same lens are used to enhance the antenna gain. Following a rigorous numerical analysis and optimization, the proposed design is fabricated and experimentally validated. The comparison of the results with the lens and without the lens illustrates that a 4 dB gain improvement is attained with the compact lens configuration. Furthermore, the antenna features a wide impedance bandwidth (S_{11}) from 24 GHz to 31 GHz and the axial ratio (AR) below 3 dB within the same operating band. The proposed design offers multiple advantages, including a simple geometrical configuration, light in weight, and ease of integration due to the planar lens structure. The proposed antenna is suitable for multiple modern communication systems, including short-range radar systems and other line-of-sight mm-wave applications requiring fixed-beam and high data rates.

Keywords Circular polarization, Planar meta-lens, Meta-lens antenna, High-gain, Wideband, mm-wave band

Due to the increasing demands for high data rate and spectrum efficiency, high-gain, wideband millimeter wave antennas have become indispensable in modern wireless communication systems. Various methods are used to improve the antenna gain and address the intrinsic challenges of the mm-wave band, that includes partial dispersion through physical obstacles, high path loss, and high interference levels. Among many gain enhancement methods, planar antenna arrays with complex feeding networks that generally involve power dividers are generally employed to improve antenna gain and directivity[1]-[2]. Additionally, electromagnetic bandgap (EBG)-based designs, multilayer antennas, and magneto-electric dipole antennas have also been explored for attaining high-gain performance. While these approaches are effective, they normally encompass geometrically and electrically complicated circuit designs and fabrication processes, which impede scalability and mass production[3]. Lens antennas are broadly known for their effectiveness in microwave and mm-wave applications. The primary ability of these antennas is to achieve high gain and broad bandwidth by concentrating electromagnetic energy into a narrow, directed beam. The conventionally used lens based on dielectric material structures generally possesses large physical dimensions, heavy weight, and relatively high fabrication costs[4–6].

To overcome the inherent limitations of traditional dielectric lenses, researchers have progressively turned to subwavelength (resonant and non-resonant) periodic structures such as frequency-selective surfaces (FSSs)[5–7] and metamaterials[8–15]. These advanced structures are effectively used to direct spherical waves into tightly focused beams, offering a promising alternative for high-performance antenna systems commonly known as meta-lens antennas. Although initially developed as transmissive converging lenses, meta-lens antennas are not

[1]Networks and Communication Engineering Department, Al Ain University, P.O. Box (112612), Abu Dhabi, UAE. [2]Engineering Optimization and Modeling Center of Reykjavik University, Reykjavik, Iceland. [3]Faculty of Electronics, Telecommunications and Informatics, Gdansk University of Technology, Gdansk 80-233, Poland. ✉email: ubaid.ullah@aau.ac.ae

limited in functionality and can implement multiple capabilities beyond those of conventional dielectric lens antennas[16]. Meta-lens antennas are capable of advanced functionalities such as spectral and polarization-based filtering of incident waves, polarization conversion, beam steering, multi-beam generation, and shaping beams into various forms[17]. Additionally, these antennas can also perform beam scanning and beam nulling when integrated into digital beamforming, analog, or hybrid networks[17–19].

Recently, several planar thin metasurface-based antennas with the operating frequency in the sub-6 GHz band and mm-wave band have been proposed[20–24]. In these works, unit cells with different physical geometries, including planar metallic patches, slots of different shapes, rings, cross-shapes, and hybrid shapes, are widely explored for different applications[24]. Designs based on planar thin metamaterial-based lenses face some inherent challenges that can considerably affect their overall performance. These include an inadequate phase control range, which limits precise wave-front shaping; material losses that reduce transmission efficiency; fabrication difficulties arising from the need for specific and often nanoscale structuring, and bandwidth limitations that impact the ability of these lenses to effectively operate over a wide frequency range[25]. All these factors pose difficulties in attaining high efficiency, precise focusing, and wide-ranging operational bandwidth in such lenses[23]. In the following discussion, we focus on three major challenges that are particularly critical to the successful implementation of these lenses. The lens should be designed to realize high gain, which is important for effective focusing and directing of electromagnetic energy, while concurrently preserving high radiation efficiency to ensure nominal energy loss and optimum overall system performance[24]-[25]. Furthermore, reducing the overall volume and maintaining an acceptable focal length to aperture diameter ratio is mandatory to counter phase quantization error. As a result, the signal experiences less degradation, which leads to improved overall system performance. This translates into an antenna with higher gain and enhanced efficiency, ensuring better signal strength and quality[23]. One of the well-known metamaterial elements is the Jerusalem cross (JC), which has been used in frequency-selective surface applications for extended periods of time. The center-connected or N-pole configuration of the JC cell offers several benefits, such as a compact footprint, flexible frequency tuning, wide bandwidth, and stable performance under wide-angle incidence when illuminated by a linearly polarized source[26,27].

This paper encapsulates two key contributions towards the design of wideband, high-gain meta-lens CP antennas. In the first stage, a wideband CP antenna excited using a single probe feeding technique is developed for illumination of the planar lens. The antenna radiator is based on the modified patch operating in the mm-wave range and radiating a wide 3 dB angular (~ 90°) beam within the antenna operating bandwidth. The wide-beam operation of the feeding antenna ensures uniform illumination of the lens. In the second stage, a new single-layer metamaterial unit cell comprising subwavelength meta-atoms arranged in a disconnected cross-shape is designed and analyzed. The four-fold symmetry of the proposed unit-cell design allows for high transmission and reduced phase errors. The transmission characteristics and the phase response of the unit cell are studied before implementing a full meta-lens structure. Based on the transmission and phase response of the unit cell design, the meta-lens antenna is implemented and analyzed numerically, followed by experimental validation of the results. The fully optimized antenna design in the first stage is used to feed the meta-lens with an aperture size of $1.7\lambda_o \times 1.7\lambda_o \times 1.7\lambda_o$, which is numerically and experimentally validated. The proposed antenna has a wide − 10 dB impedance bandwidth and axial ratio (AR ≤ 3) dB of more than 7 GHz. The proposed meta-lens boosts the realized gain of the antenna by more than 4 dB with a reasonable F/D ratio. The impedance and axial ratio bandwidths of the antenna are approximately 26% with the center frequency of 27.5 GHz.

Feed antenna design and analysis

Feeding antennas are a crucial consideration for lens-based devices. In this study, a new circularly polarized planar antenna with wideband characteristics and a stable radiation pattern is designed. The proposed design is implemented on a Rogers RO4003 substrate with a dielectric constant of 3.38 and a thickness of 0.813 mm. The geometry of the feeding antenna with all its geometrical parameters is shown in Fig. 1. The antenna is comprised of a systematically modified V-shape patch structure excited with a probe extended from a coaxial line through the ground plane shown on the right of Fig. 1(a). The impedance matching between the feeding probe and the radiator is achieved by adjusting the probe position. For wideband impedance matching, the optimum feed point is positioned at x = 2.5 mm and y = 0.2 mm. The coordinate system origin is localized at the center of the substrate ($W_s/2$, $L_s/2$), with the x-axis orientation along the horizontal edge and the y-axis along the vertical edge of the substrate, as shown. To further improve the reflection coefficient of the feeding antenna, a small diagonal slot of the width of 0.59 mm and the length of 1.974 mm is etched near the feeding point. This structural modification alters the local current distribution and introduces supplementary capacitive and inductive effects, which lead to improved impedance matching and reduced return loss. The discontinuity introduced by the slots helps in improving the axial ratio of the antenna by redistributing surface currents, thereby enhancing the generation of orthogonal field components required for circular polarization.

To elaborate on the antenna operating mechanism, the surface current distributions are shown in Fig. 1 (b). For a clear illustration of the field distribution, the modified patch structure is aligned with *the x*-axis and *y*-axis. At 0°, the dominant current is oriented in the + *x*-axis, showing the Quasi-TM_{10} mode. While for the 90°, the vector fields are predominantly aligned along the + *y*-axis, indicating the excitation of the Quasi-TM_{01} mode. Similarly, for the 180°, the orientation of the vector fields is along the –*x*-axis, reflecting the 180° phase variation of the Quasi-TM_{10} mode at that time instant. And lastly, at the 270°, the fields are aligned along the –*y*-axis. The Quasi-TM_{10} and Quasi-TM_{01} modes are similar to the standard TM modes but slightly altered due to the modified shape and size of the patch antenna. The rotation of the fields with different angular times clearly indicates the excitation of the right-hand circular polarization. It is noted that the geometrically modified patch enables simultaneous excitation of the Quasi-TM_{10} and Quasi-TM_{01} modes. The Quasi-TM_{01} and Quasi-TM_{10} modes are the key modes responsible for the circular polarization in the proposed antenna. While the overall

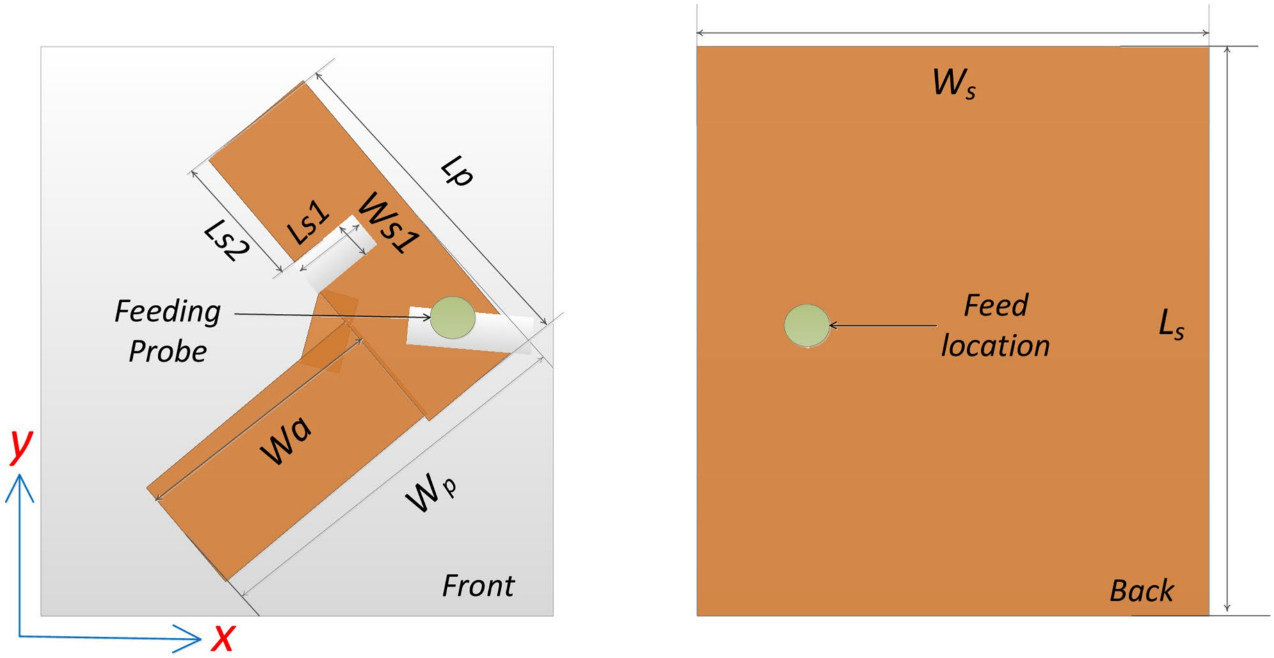

(a)

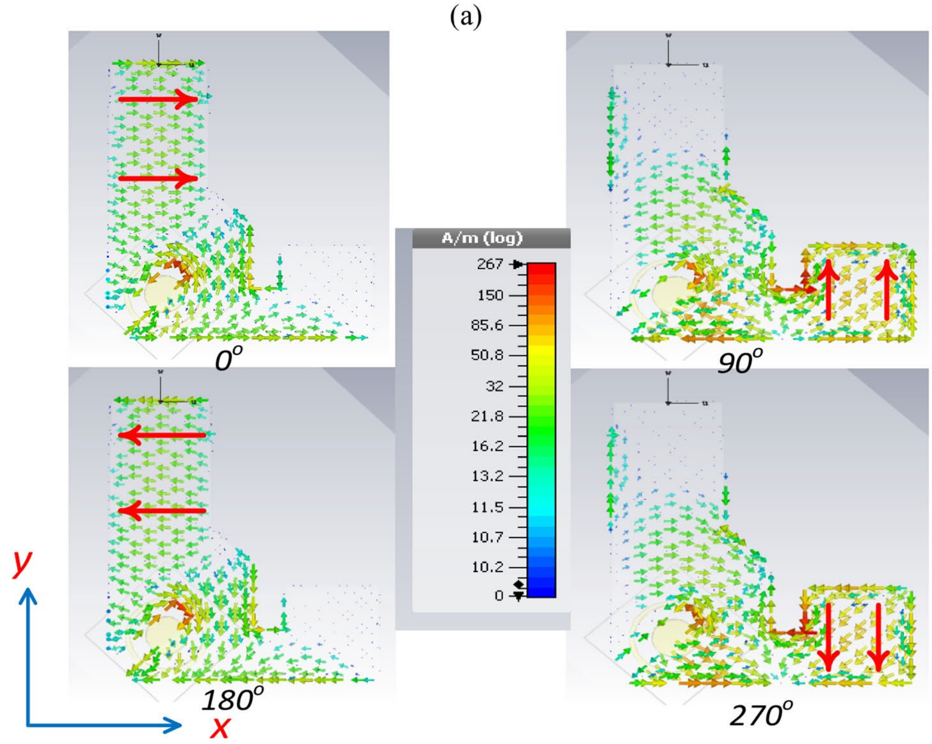

(b)

Fig. 1. (**a**) The proposed probe-fed circular polarized wideband antenna with its geometrical parameters: L_s = 11 mm, W_s = 8.7017 mm, L_p = 5.411 mm, W_p = 4.041 mm, L_{s1} = 1.046 mm, W_{s1}= 0.737 mm, L_{s2} = 1.98 mm, W_a = 3.015 mm. (**b**) Current distribution at different angular times.

current distribution may show contributions from other minor modes, the CP behavior is primarily governed by the superposition of Quasi-TM_{01} and Quasi-TM_{10}.

Following a full-wave optimization of the feeding antenna's geometrical parameters, the design is further extended to a two-element (not shown for brevity) configuration to enhance its performance characteristics, particularly its realized gain. To realize the two-element design and to accommodate the second antenna, the substrate is extended along the length in the y-direction. The antenna is then replicated and rotated using the same dimensions at an approximately half-wavelength distance to ensure an acceptable level of mutual coupling and spatial/polarization diversity. The absolute current magnitude of the two-element configuration in the same phase is shown in Fig. 2(d). The upper part of the figure presents the surface current distribution when port 1 is excited, while the lower part shows the distribution when port 2 is excited. The minor induced current on the non-excited element clearly confirms minimal mutual coupling between the two antennas, leading to enhanced isolation. Figure 2 shows the comparison of the single-element (SE) antenna and the two-element

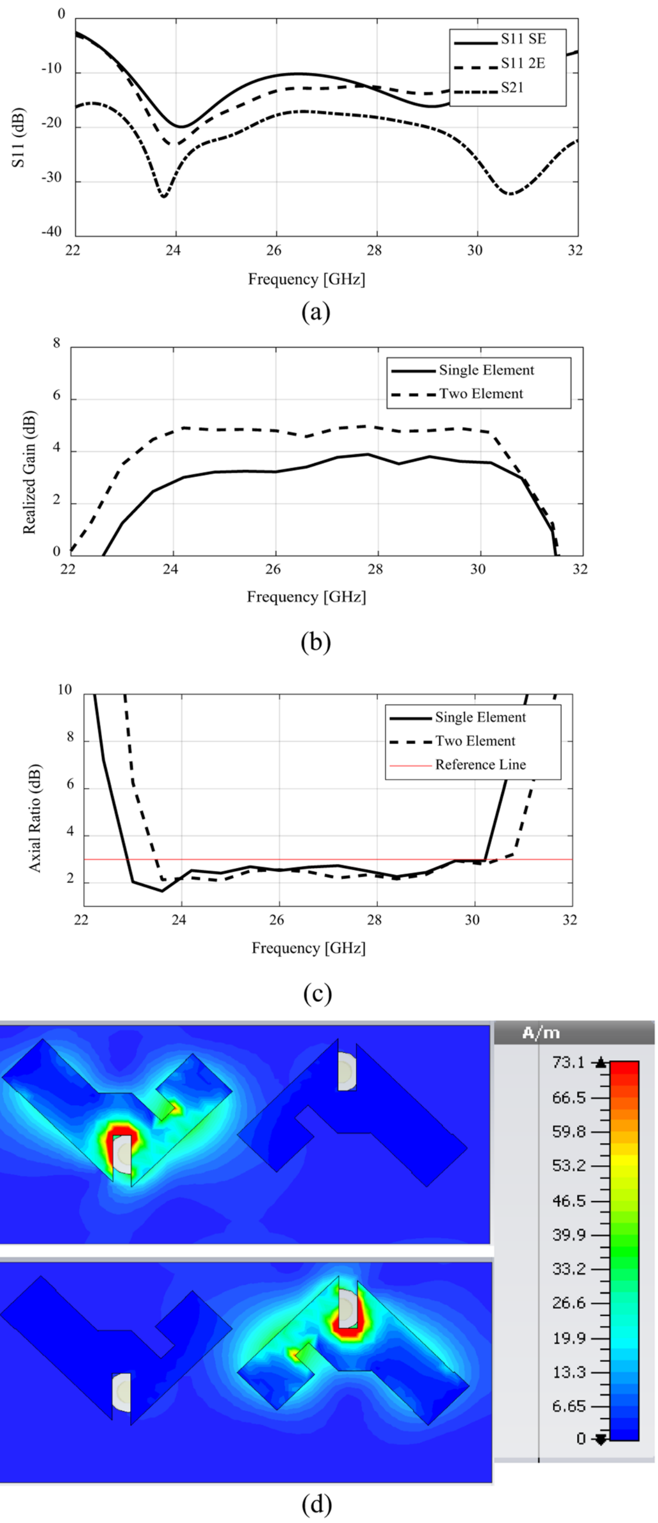

Fig. 2. Characteristics of the feeding antenna without the lens: (**a**) reflection coefficient ($|S_{11}|$), (**b**) axial ratio, (**c**) realized gain, and (**d**) Surface current on two elements (port 1: top, port 2: bottom).

(2E) design without the lens. The reflection coefficient (S_{11}) illustrated in Fig. 2(a) of both designs remains nearly identical and shows a wideband response from 23 GHz to about 30 GHz. The mutual coupling between the two elements is characterized by the S_{21} parameter, which shows an average value of approximately − 18 dB within the operating band as illustrated in the corresponding figure.

The axial ratio of both designs remains consistent with a slight upward shift in frequency for the 2E design as depicted in Fig. 2(b). The AR response indicates that the circular polarization performance is maintained across the two configurations within the same frequency band as that of the impedance matching. Figure 2(c) also includes the comparison between the realized gain of the single- and two-element designs. Compared to the two-element design, the single-element design has an average realized gain of 3.4 dBi within the operating bandwidth, whereas the two-element design has an average gain of 4.8 dBi, underscoring a gain enhancement of approximately 1.4 dBi. The gain of the two-element array is limited by back radiation and mutual coupling between the elements, which reduces the amount of power directed in the forward direction. Furthermore, it is imperative to mention that the probe-fed patch excites the Quasi-TM mode, which yields a broadside radiation pattern with a wide beam[28]. The in-band 3 dB angular beamwidth of the proposed design without the lens is 90° on average, which is highly desirable for constant illumination of the lens.

Meta-lens unit cell design and analysis

The geometry and physical dimensions of the proposed meta-lens unit-cell design are shown in Fig. 3. Two pairs of metallic strips are positioned at a controlled distance d from each other to form a disconnected cross-shape unit-cell design with four-fold symmetry. The vertical strips pair aligned along the *y*-axis and the horizontal pair along the *x*-axis are symmetrically placed with respect to the center of the unit cell. The rectangular metallic strips are patterned on a low-loss Rogers RO4003 dielectric substrate with a relative permittivity of 3.38 and a thickness of 0.813 mm. The proposed unit cell has four-fold rotational symmetry and spatial discontinuity that reduces potential phase errors caused by polarization and facilitates high transmission with both preserved and manipulated circular polarization states. To achieve the phase compensation and wave-front shaping needed for gain enhancement and beam focusing in CP-fed lens antenna systems, a full meta-lens is implemented. The unit cell is periodically arranged in a 2D-square-lattice with a periodicity $P = 5.714$ mm, which corresponds to $0.514\lambda_o$ at 27 GHz to form the meta-lens.

The proposed unit cell is simulated under normal and oblique plane-wave excitation using CST Microwave Studio. The unit cell's geometry is optimized to perform efficiently in the target frequency band (24–30 GHz) by controlling the geometrical parameters *Lm*, Wm, and the separation distance *d*. The periodicity parameter of the full square lattice is tuned to achieve the desired electromagnetic performance after the unit cell optimization. The linear transmission coefficient and the transmission phase of the optimized unit-cell under normal incidence are illustrated in Fig. 4. The simulation results indicate a high transmission level, averaging 90%, across the operating frequency band with minimal variation. The transmission phase response illustrated in the same figure depicts a stable phase in the entire operating bandwidth of the antenna. The average phase range of the unit-cell is 130° with a slower phase slope reflecting low susceptibility to phase error over a wideband. In addition, the unit-cell is investigated under oblique incidence (5° to 30°), with the corresponding transmission magnitude and phase responses shown in Fig. 5.

The results indicate that with the increasing incidence angle increases between 5° and 30° in 5° steps, the phase response shows a slightly steeper slope, which results in an average phase shift of almost 20°. On the contrary, the transmission coefficient is only slightly influenced by the incidence angle, with an average loss of

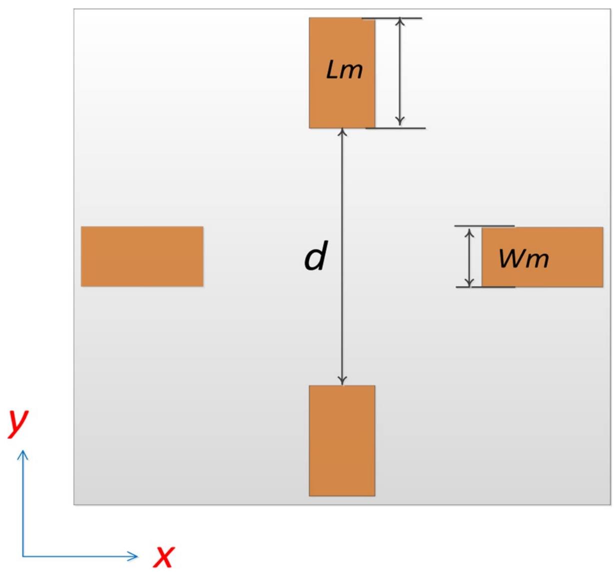

Fig. 3. Configuration of the proposed unit-cell design with geometrical parameters: W_m = 0.3001 mm, L_m = 0.63395 mm, and $d = 3.31040$ mm.

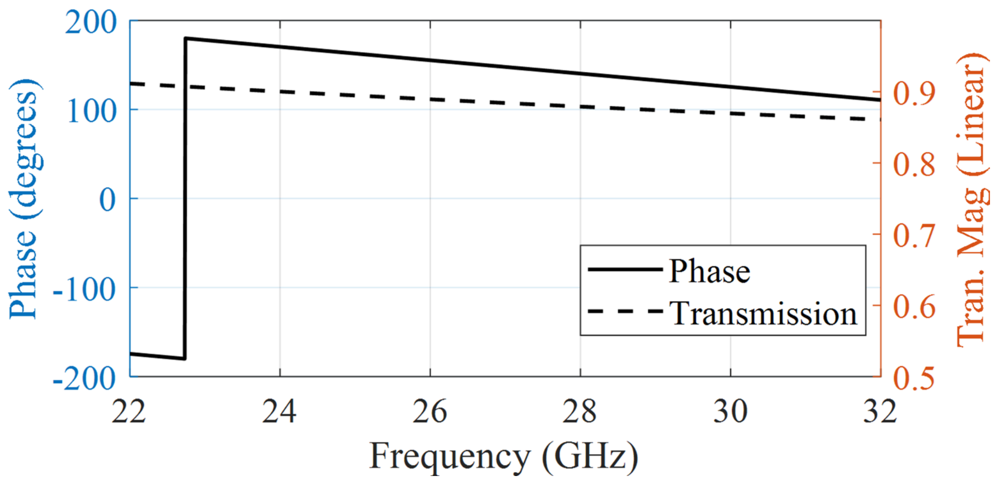

Fig. 4. Simulated performance matrix of the proposed unit-cell design, transmission phase (solid), and transmission magnitude (dashed).

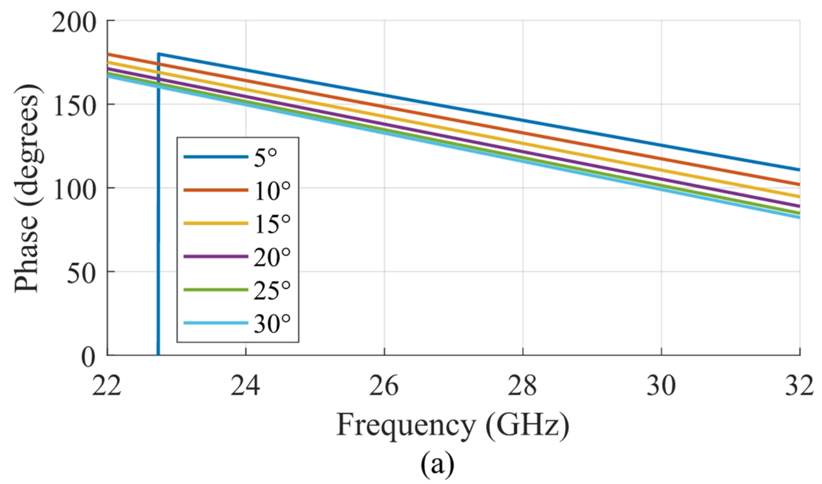

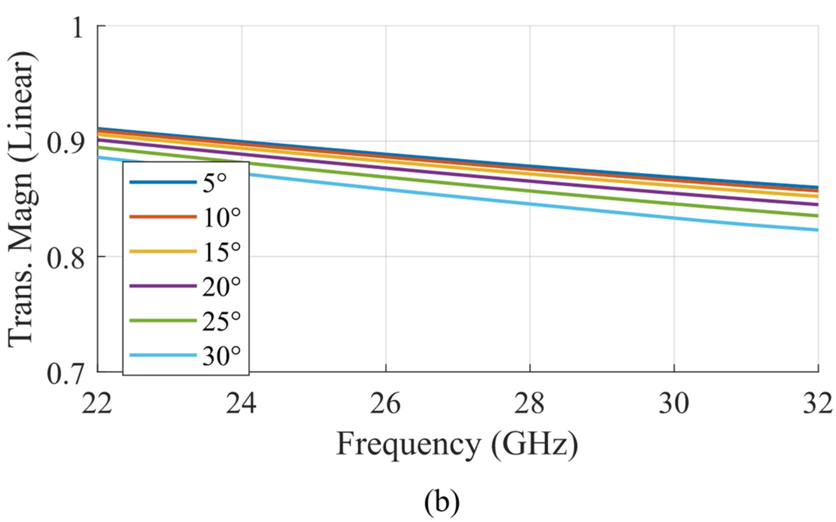

Fig. 5. Simulated performance matrix of the proposed unit-cell design under oblique incidence, (**a**) transmission phase, and (**b**) transmission magnitude.

about 5% over the wide operating bandwidth. The unit cell is shown to maintain high transmission efficiency and angular stability, confirming its suitability for wideband transmissive applications under oblique incidence.

Meta-lens antenna

Figure 6 shows the 2D square lattice of the proposed lens and the schematic of the lens antenna, which is centrally illuminated by the wideband circularly polarized (CP) antenna developed in the first design stage. The 3 × 3 metamaterial flat square lens with length $D = 20$ mm, shown in the top section of Fig. 6, is positioned at a focal distance of $F = 20$ mm, which corresponds to approximately $1.8\lambda_o$ at 27 GHz from the source antenna as illustrated in the bottom section of Fig. 6. A comprehensive numerical study of the single-layer meta-lens configuration reveals notable improvement in the realized gain of the antenna. With the introduction of the meta-lens, the antenna gain is effectively enhanced by collimating the radiated fields, which focuses energy into the main beam, resulting in an improved directivity.

Working mechanism of the meta-lens antenna

In this section, the working mechanism of the proposed meta-lens antenna is investigated through an analysis of the aperture-plane electric-field magnitude and the relative phase variation of the electric-field components E_x and E_y along the z-direction. Figure 7(a) illustrates the electric-field magnitude on the aperture plane for the single-layer meta-lens. The field strength is highest near the center and gradually decreases toward the edges, mainly due to the radiation pattern of the circularly polarized feeding antenna, which illuminates the central region more effectively. After transmission through the meta-lens, the field shows a clear forward concentration, indicating that part of the radiated energy is redirected toward the broadside direction. However, the non-uniform field distribution across the aperture suggests that the effective aperture is only partially utilized in the single-layer configuration. The corresponding two-dimensional phase distribution is shown in Fig. 7(b). A relatively smooth phase profile is observed near the aperture center, indicating partial compensation of the spherical wave-front emitted by the CP feed. In contrast, larger phase deviations appear toward the aperture edges, reflecting residual phase errors caused by the limited phase control of a single metasurface layer. As a result, a partially planar wave front is achieved with the single layer. Figure 7(c) shows the phase variation along the aperture center line, which further clarifies this behavior. The phase remains relatively flat near the center but shows a large deviation toward the edges of the aperture. This confirms that the single-layer meta-lens offers only partial wave-front shaping, where the central aperture region contributes more effectively to constructive broadside radiation, while the phase alignment remains less on the edges.

Moreover, the same analysis is extended to the two-layer configuration of the antenna. Figure 7(d) presents the electric-field magnitude on the aperture plane for the double-layer meta-lens. Compared to the single-layer design, the field is noticeably stronger and more evenly spread across the entire aperture. This indicates that the double-layer structure is better at capturing the circularly polarized energy from the feed and distributing

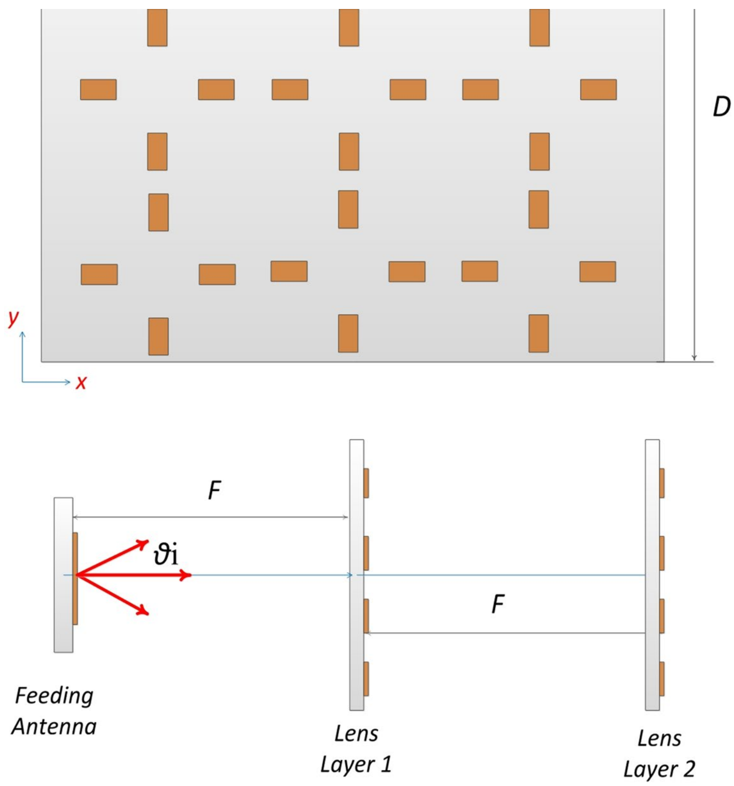

Fig. 6. Schematics of the proposed lens antenna: lens front view (top), side view (bottom).

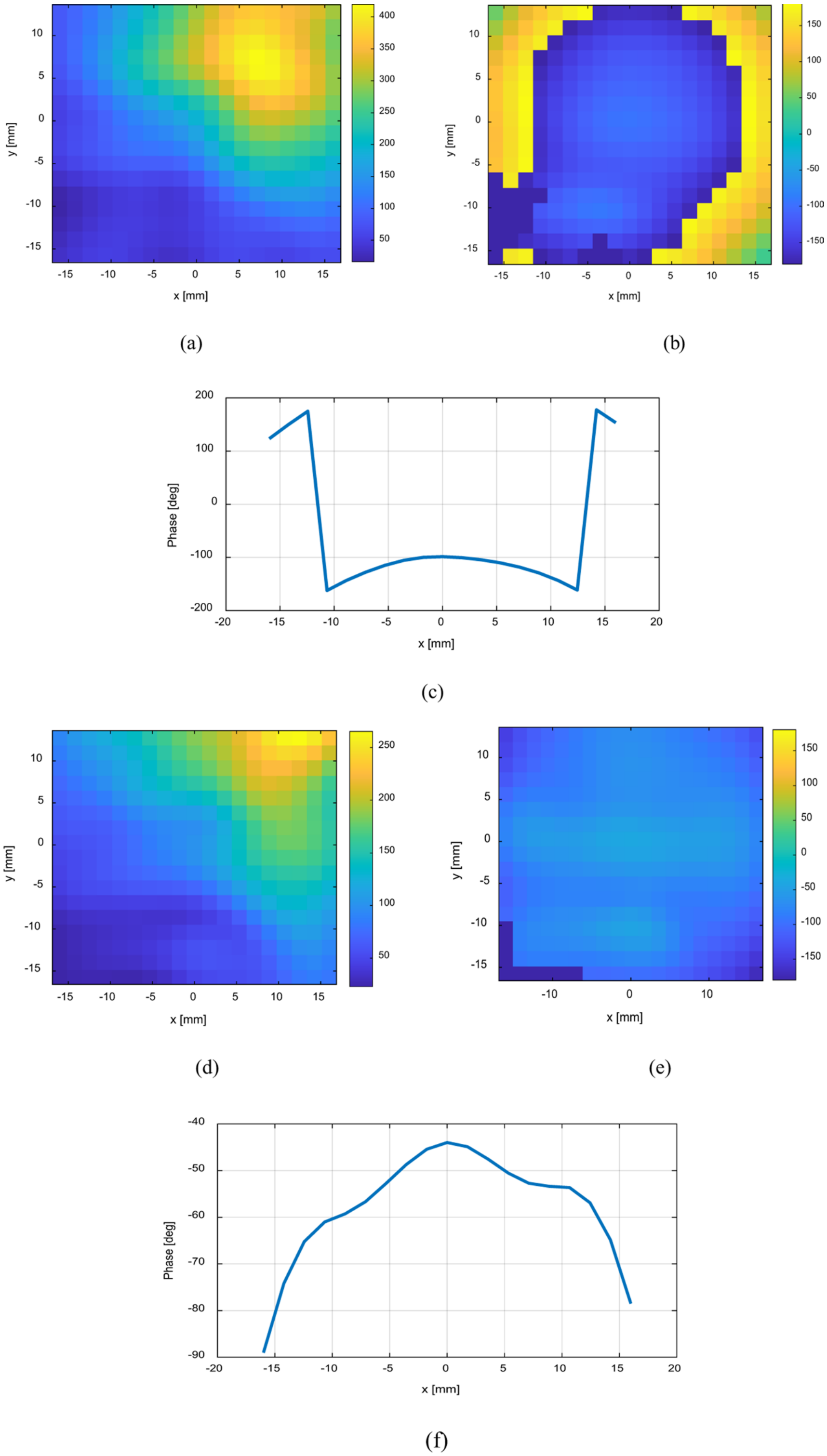

Fig. 7. Aperture-plane electric-field magnitude and phase distributions for the proposed meta-lens antenna: (**a**) electric-field magnitude, (**b**) two-dimensional phase distribution, and (**c**) phase variation along the aperture center line for the single-layer meta-lens; (**d**) electric-field magnitude, (**e**) two-dimensional phase distribution, and (**f**) phase variation along the aperture center line for the double-layer meta-lens.

it efficiently over the aperture, which results in higher aperture efficiency. The corresponding two-dimensional phase distribution is shown in Fig. 7(e). A clear improvement in phase uniformity can be seen, with a larger area of nearly constant phase extending closer to the edges of the aperture. This improved phase behavior confirms that the additional metasurface layer enhances spatial phase control, enabling a more effective conversion of the spherical circularly polarized wave-front into a quasi-planar wave-front. Figure 7(f) shows the phase variation along the center line of the aperture, further confirming the near-constant phase profile. In comparison with the single-layer meta-lens, the phase remains more stable across the aperture, and the phase distortion near the edges is significantly reduced. As a result, the fields radiated from different parts of the aperture combine more constructively in the far field, leading to higher directivity and an improved realized gain. In short, the gain enhancement of the proposed meta-lens is primarily attributed to its ability to reshape the radiated wave-front and concentrate energy in the desired direction. By transforming the naturally diverging radiation from the feed into a more collimated beam, the meta-lens increases the effective aperture and improves radiation directivity. This redistribution of energy reduces power leakage into undesired directions and enhances overall radiation efficiency, resulting in a noticeable gain improvement.

Gain and radiation characteristics for various F/D ratios

To determine the realized gain performance of the proposed meta-lens antenna, different focal-length-to-diameter *(F/D)* ratios are analyzed, as shown in Fig. 8. As seen, the *F/D* ratio of 0.9 results in the highest peak gain, whereas *F/D* = 1 offers a more stable gain response over a wider bandwidth within the antenna operating band. Moreover, *F/D* ratios of 0.8 and 1.1 exhibit gain enhancement within a narrow bandwidth, which may be attributed to suboptimal phase alignment across the aperture, resulting in destructive interference of the radiated field. This basis is extended to create a two-layer configuration that has layers at successive focal distances (*F* = 20 mm and *F* = 40 mm). The implementation of a two-layer planar lens configuration enhances beam collimation and refines the transmitted wave front (see Fig. 7), resulting in improved directivity and a further improvement in the antenna's realized gain.

Figure 9 illustrates the simulated realized gain of the antenna for four different configurations in the xy- and xz-plane evaluated at the center frequency. The blue dashed line represents the realized gain of the single-element antenna (SEA) without the lens (SEA-WOL), which shows ~ 4 dB gain. The green solid line shows the SEA with one layer of the lens (SEA-1LL) and a 0.9 F/D ratio. The realized gain for this configuration is approximately 6 dBi, indicating a 2 dB gain enhancement in both planes. The red curve (SEA-2LL) shows the realized gain of the antenna when the two layers of the lens are illuminated with SEA at successive focal distances. The configuration enhances the gain by more than 4 dBi compared to the antenna without the lens. Finally, the black curve (2EA-2LL) illustrates the two-element antenna illuminating the two layers of the lens, improving the gain by more than 6 dBi. Although configurations with three or more layers were explored, they offered only a very small increase in gain. Furthermore, adding more layers would increase insertion losses, overall thickness, and fabrication complexity. Therefore, the two-layer design was selected as a trade-off between gain enhancement, efficiency, and practical feasibility. After adding the meta-lens, the calculated aperture efficiency of the antenna is about 22%, and the total aperture efficiency (including typical spillover efficiency, patch antenna loss term, illumination efficiency, phase efficiency, and lens material/reflection loss) is approximately 34%, showing that the physical aperture is being used effectively to improve the gain of the antenna. At the same time, the overall radiation efficiency remains approximately 90%, so most of the input power is still being radiated.

Results and discussion

The proposed antenna is experimentally validated in a fully calibrated anechoic chamber. The fabricated prototype of the single-element source antenna is shown in Fig. 10 (a). To avoid field distortion due to the dielectric nature of the mechanical support, the substrate is extended along the x-axis. To maintain the required focal distance between the feeding antenna and the lens layer, 3D-printed plastic spacers were employed to accurately maintain the required spacing and *F/D* ratio. The current dielectric size is chosen to ensure the mechanical stability of the prototype; however, this results in some phase errors and additional losses, which have adverse effects on the antenna's efficiency and boresight gain. The lens layer, side view of the assembled meta-lens antenna, and the in-chamber view are shown in Figs. 10 (b) through 10(d), respectively. To validate the design experimentally, only the single antenna configuration for feeding the lens was fabricated. This allows for a simple and cost-effective setup, minimizing fabrication complexity and alignment challenges while being sufficient for the antenna performance validation.

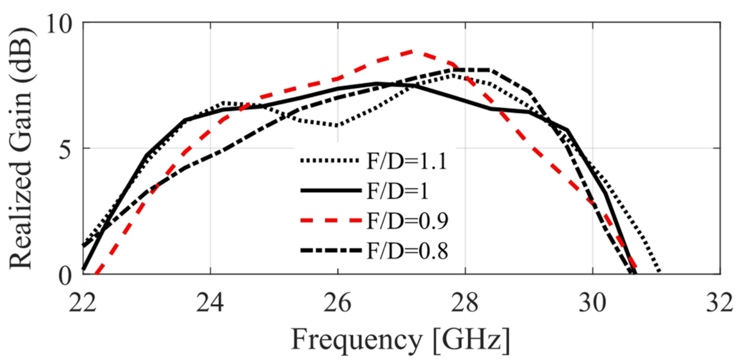

Fig. 8. Realized gain analysis with different F/D ratios.

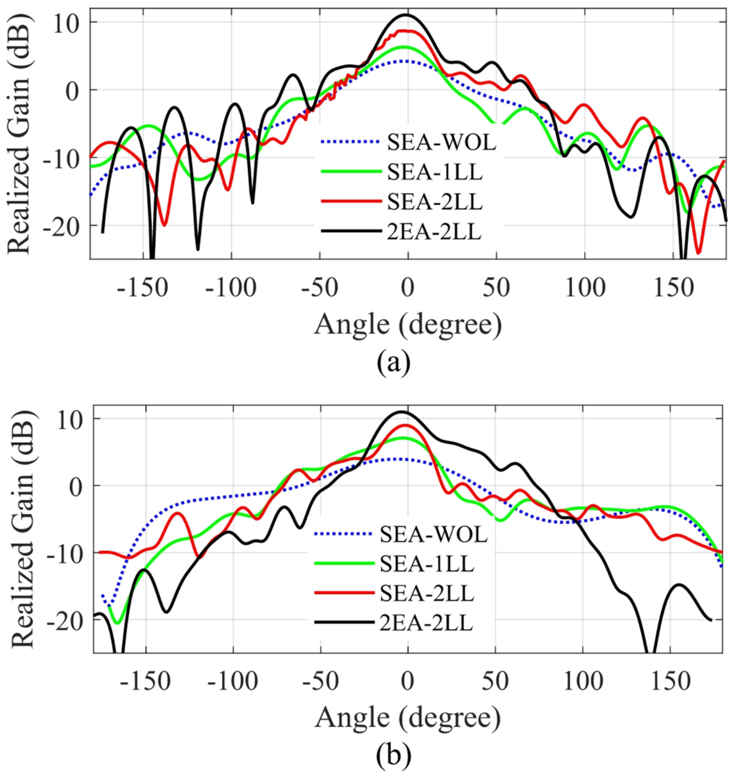

Fig. 9. Realized gain analysis with different configurations of the meta-lens antenna: (**a**) *xy*-plane, and (**b**) *xz*-plane.

The simulated and measured return loss of the meta-lens antenna is shown in Fig. 11 (a). Both responses show a good impedance matching in the antenna working band from 24 GHz to approximately 31 GHz. The presence of the dielectric material (used for mechanical support) near the feed slightly alters the local permittivity, resulting in the frequency shift and improved impedance matching and S_{11} across the operating band. Both the simulation and measured results clearly indicate the wideband operation of the proposed antenna. Figure 11(b) shows the simulated and measured axial ratio of the lens antenna. The simulated and measured results indicate that the axial ratio remains below the 3 dB reference level throughout the entire impedance bandwidth of the antenna, confirming the polarization stability of the lens as it retains circular polarization over the operational frequency range. The numerical and experimental results are in close agreement. Moreover, Fig. 11(c) shows the realized gain of the meta-lens antenna. The simulated and measured results exhibit a stable gain response over a wide bandwidth, confirming the effective wideband operation of the proposed meta-lens antenna. While operating with circular polarization (CP), the antenna achieves a peak gain of approximately 9 dBi and maintains an average gain of around 7.7 dBi between 24 GHz and over 30 GHz.

Figure 12 presents the simulated and measured radiation patterns of the antenna in the xy- and xz-planes at three distinct frequencies. The co-polarized radiation corresponds to right-hand circular polarization (RHCP), while the cross-polarized pattern represents left-hand circular polarization (LHCP). In the broadside direction, the co-polarized fields are, on average, 20 dB stronger than the cross-polarized fields, indicating high polarization purity. Slightly higher cross-polarization levels are observed at off-axis angles, which can be attributed to edge effects, non-uniform aperture fields, and the phase manipulation by the meta-lens. These off-axis effects do not affect the antenna's performance in the broadside direction, where the radiation is strongest. The radiation beams are nearly symmetrical at all evaluated frequencies, further confirming the consistent performance of the antenna. These results also demonstrate that the proposed meta-lens effectively preserves the sense of polarization across the operational bandwidth. Additionally, the minimum difference between the main lobe and the highest side lobe is more than 10 dB, indicating that the side-lobe levels are within acceptable limits.

Benchmarking

Table 1 provides a detailed benchmarking of the proposed meta-lens antenna against the state-of-the-art designs. The comparison focuses on key performance metrics such as antenna type, aperture dimensions, gain enhancement, aperture efficiency, unit cell count, material specifications, and substrate characteristics. The proposed antenna clearly outperforms many previous designs by combining wide bandwidth, high aperture efficiency, and a compact size, all while keeping the structure simple and practical. Traditional patch antennas, like the one in[4], are very narrowband and only provide small gain improvements. On the other hand, wideband solutions such as log-periodic dipole arrays[29] or horn antennas[31] achieve larger bandwidths but need very large apertures and many elements, making them bulky, complex, and difficult to manufacture. Other designs, like

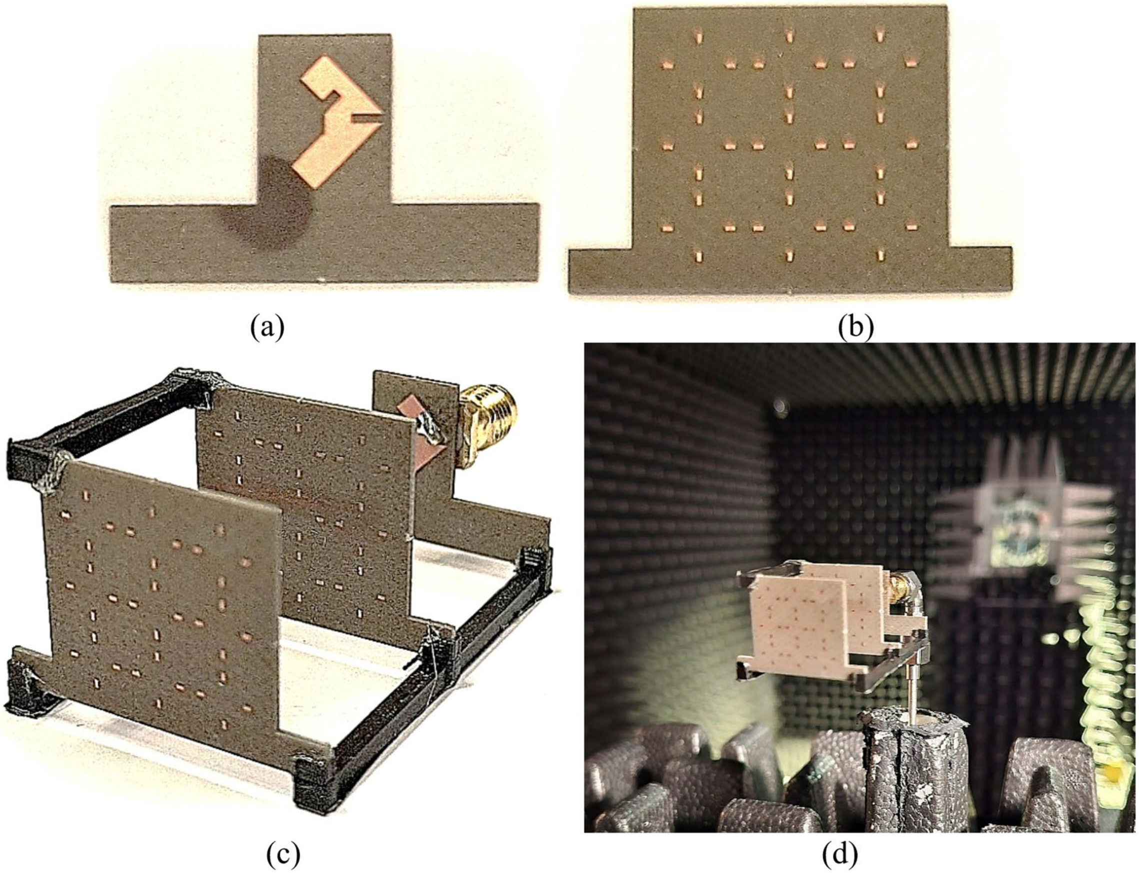

Fig. 10. Photograph of the proposed meta-lens antenna prototype; (a) feeding antenna, (b) lens, (c) perspective view, and (d) in-chamber view.

cylindrical or metasurface-based antennas[17], often use thick substrates or large arrays, which either waste the aperture or give only modest performance improvements.

In contrast, our modified patch antenna achieves a 26% impedance bandwidth with circular polarization in a compact 1.6λ × 1.6λ aperture, giving a 4.3 dBi gain improvement and 22% aperture efficiency. This is done with just a 3 × 3 array of metallic strips on a thin, low-loss substrate, reducing dielectric losses and simplifying fabrication. Overall, the antenna combines wideband performance, efficient use of the physical aperture, and structural simplicity, making it very suitable for modern compact broadband wireless applications and outperforming many previous designs in both efficiency and practicality.

Conclusion

In this paper, a wideband, circularly polarized, high-gain meta-lens antenna is proposed and thoroughly investigated. A compact feed antenna was first designed to efficiently illuminate the planar meta-lens, providing circular polarization, broad beamwidth, and a simple excitation method for easy fabrication. The meta-lens, composed of four-fold symmetrical metallic strips in a disconnected cross configuration, effectively collimates the radiated fields while preserving polarization and maintaining stable phase characteristics across the operating band. The complete antenna achieves a wide 26% impedance bandwidth from 24 to 30 GHz while maintaining an axial ratio below 3 dB, and the integrated design boosts the gain by more than 4 dB without disturbing the radiation pattern. Traditional patch antennas are typically narrowband, while log-periodic and horn antennas require large apertures and many elements, making them bulky and difficult to implement. Other cylindrical or metasurface-based designs often depend on thick substrates and do not fully use the available aperture. In contrast, this design achieves wideband operation and improved gain using only a simple 3 × 3 array of metallic strips on a thin, low-loss substrate. Overall, the antenna offers good performance, easy fabrication, and a compact footprint, making it a practical choice for modern high-frequency wireless systems. The limitation of the proposed design is that gain improvement requires multiple metasurface layers, which increases the geometrical complexity and thickness of the antenna system.

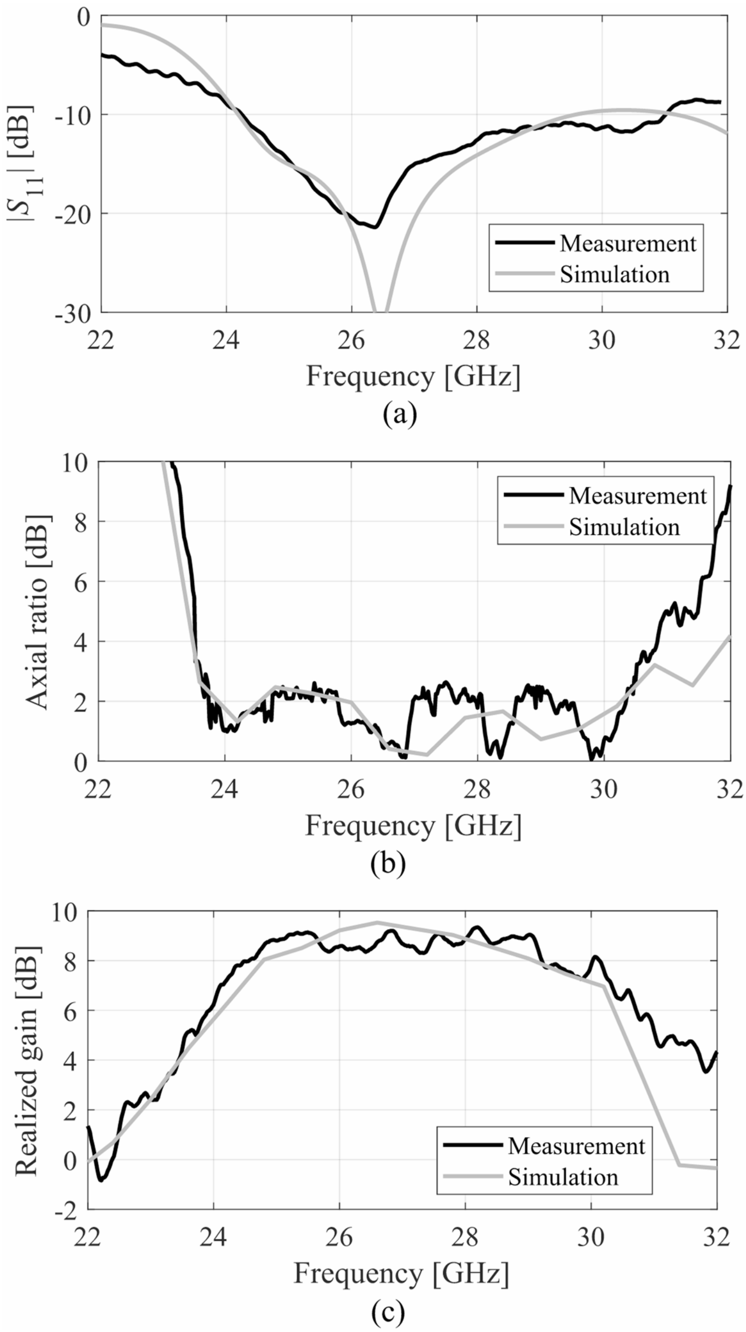

Fig. 11. Simulated and measured performance matrix of the proposed meta-lens antenna (**a**) return loss $|S_{11}|$, (**b**) axial ratio, (**c**) realized gain.

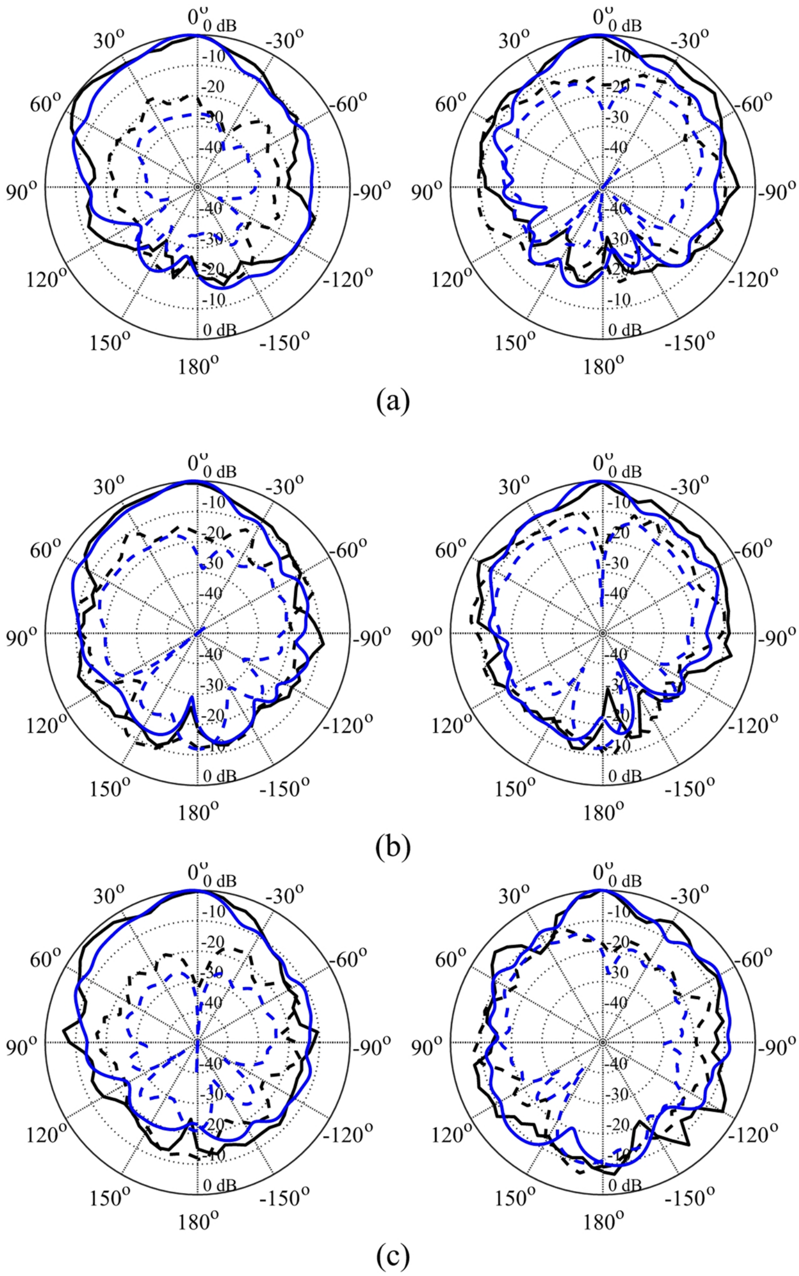

Fig. 12. Simulated (blue) and measured (black) radiation pattern at different frequencies in the *xy*-plane (right), and *xz*-plane (left). (**a**) 26 GHz, (**b**) 28 GHz, and (**c**) 30 GHz.

Ref	Antenna type	Impedance bandwidth (%)	Polarization	Aperture Dimensions (λo × λo)	Gain improvement (dBi)	Aperture Efficiency (%)	No. of Unit cells/layers	Material type	Substrate height h, ε_r
[4]	Patch	5	LP	----	3.9	----	12 × 7 (L1)	Metallic lines	FR4, 1.6, 4.4
[29]	Log-periodic dipole array	42	LP	1.3 × 2	4	19	83	C-Shaped Resonator	RT, 0.5, 2.2
[17]	Cylindrical Antenna	17.4	LP	1.9 × 1.9	3.5	----	7 × 7	Squared metal lattice	FR4, 10, 4.4
[30]	Horn	25	LP	15.8 × 15.8	----	13.8	40 × 40	Cross-shape	F4B, --, 2.55
[31]	Horn	17.5	DP	10 × 10	---	19.5	20 × 20	Square ring with L-shape	RT, 1.54, 3.35
[32]	ME Dipole	12.5	LP	5.7 × 5.7	---	20.5	12 × 12	C-shaped resonator	RT, 0.8, 3.55
prop	Modified patch	26	CP	1.6 × 1.6	4.3	22	3 × 3	Metallic strips	RT, 0.813, 3.38

Table 1. Comparison with state-of-the-art benchmark designs.

Data availability
All data generated or analyzed during this study are reported in the manuscript.

Received: 22 December 2025; Accepted: 10 April 2026
Published online: 02 May 2026

References
1. Aeini, M., Jarchi, S. & Faraji-Dana, R. Compact, wideband-printed quasi-Yagi antenna using spiral metamaterial resonators. *Electron. Lett.* **53** (21), 1393–1394 (2017).
2. Ali, A., Ahmad, A. & Alam, M. High gain metamaterial implemented antenna design with circular polarization for mm-Wave 5G and 6G sub-THz communication. *J. Electron. Inf.* **5** (4), 423–441 (2023).
3. Ali, J., Ahmad, A. & Choi, D. Single-layer metasurface-based reflectarray antenna with H-shaped slotted patch for X-band communication. *Nanomaterials* **14** (18), 1495 (2024).
4. Bayat, M. & Khalilpour, J. A high gain miniaturised patch antenna with an epsilon near zero superstrate. *Mater. Res. Exp.* **6** (4), 1–9 (2020).
5. Cai, T. et al. Compact microstrip antenna with enhanced bandwidth by loading magneto-electro-dielectric planar waveguided metamaterials. *IEEE Trans. Antennas Propag.* **63** (5), 2306–2311 (2015).
6. Cai, Y. M., Li, K., Yin, Y. Z. & Hu, W. Broadband circularly polarized printed antenna with branched microstrip feed. *IEEE Antennas Wirel. Propag. Lett.* **13**, 674–677 (2014).
7. Chen, M., Jiang, H., Zhang, H., Li, D. & Wang, Y. Design of an acoustic superlens using single-phase metamaterials with a star-shaped lattice structure. *Sci. Rep.* **8**, 1–8 (2018).
8. Chen, W. T. A broadband achromatic metalens for focusing and imaging in the visible. *Nat. Nanotechnol.* **13** (3), 220–226 (2018).
9. N. Chen, Z. Microwave metalens antennas. *Proc. IEEE.* **111** (8), 978–1010 (2023).
10. Erfani, E., Niroo-Jazi, M. & Tatu, S. A high-gain broadband gradient refractive index metasurface lens antenna. *IEEE Trans. Antennas Propag.* **64** (5), 1968–1973 (2016).
11. Esmail, B. A. F., Koziel, S. & Szczepanski, S. Overview of planar antenna loading metamaterials for gain performance enhancement: the two decades of progress. *IEEE Access.* **10**, 27381–27403 (2022).
12. Fathipour, M. et al. Design and fabrication of a multilayer metamaterial antenna with high-gain and good radiation patterns for WiFi and WiMAX applications. *IET Commun.* **17**(4), 448–459 (2023).
13. Guo, Q. Y. & Wong, H. A millimeter-wave Fabry–Pérot cavity antenna using Fresnel zone plate integrated PRS. *IEEE Trans. Antennas Propag.* **68** (1), 564–568 (2020).
14. He, Z., Jin, J., Zhang, Y. & Duan, Y. Design of a two-dimensional T-shaped metamaterial with wideband, low loss. *IEEE Trans. Appl. Supercond.* **29** (2), 1–4 (2019).
15. Lawrance, J. E., Christodoulou, C. G. & Taha, M. R. A high-power microwave zoom antenna with metal-plate lenses. *IEEE Trans. Antennas Propag.* **63** (8), 3380–3389 (2015).
16. Li, H. Dual-band Fresnel zone plate antenna with independently steerable beams. *IEEE Trans. Antennas Propag.* **66** (4), 2113–2118 (2018).
17. Luo, M., Sang, X., Tan, J. & Chen, J. A novel miniaturized metamaterial lens antenna. *Int. J. RF Microw. Comput. -Aided Eng.* **30** (7), 1–8 (2020).
18. Meng, Y. et al. Countering single-polarization radar based on polarization conversion metamaterial. *IEEE Access.* **8**, 206783–206789 (2020).
19. Nayeri, P. 3D printed dielectric reflectarrays: Low-cost high-gain antennas at sub-millimeter waves. *IEEE Trans. Antennas Propag.* **62** (4), 2000–2008 (2014).
20. Sadeqi, A., Nejad, H. R., Owyeung, R. E. & Sonkusale, S. Three dimensional printing of metamaterial embedded geometrical optics (MEGO). *Microsyst. Nanoeng.* **5** (1), 16 (2019).
21. Shastri, A. 3D printing of millimetre wave and low-terahertz frequency selective surfaces using aerosol jet technology. *IEEE Access.* **8**, 177341–177350 (2020).
22. Sun, Y., Du, Z., Du, J., Liu, Y. & Basit, M. A. Enhanced gain and broadband of endfire antenna by using I-shaped resonator structures. *Int. J. RF Microw. Comput. -Aided Eng.* **28** (7), 1–6 (2018).
23. Ullah, U., Koziel, S. & Mabrouk, I. B. Rapid redesign and bandwidth/size tradeoffs for compact wideband circular polarization antennas using inverse surrogates and fast EM-based parameter tuning. *IEEE Trans. Antennas Propag.* **68** (1), 81–89 (2020).
24. Ullah, U., Koziel, S. & Pietrenko-Dabrowska, A. Characteristics mode analysis and excitation of orthogonal modes on a single substrate for wideband IoT applications in the millimeter wave band. *Sci. Rep.* **15**, 8810 (2025).
25. Ullah, U., Koziel, S., Pietrenko-Dabrowska, A. & Kamal, S. Characteristics mode analysis of a unit-cell and a 3×3 finite metasurface design for IoT applications in the mm-wave band. In: *Proc. 11th Int. Conf. Internet of Things: Systems, Management and Security (IOTSMS)*, Malmö, Sweden, 38–43 (2024).
26. Wu, G. B. A universal metasurface antenna to manipulate all fundamental characteristics of electromagnetic waves. *Nat. Commun.* **14** (1), 5155 (2023).

27. Wu, G. B., Qu, S. W. & Yang, S. Low-profile transmitarray antenna with Cassegrain reflectarray feed. *IEEE Trans. Antennas Propag.* **67** (5), 3079–3088 (2019).
28. Wu, G. B. et al. 3D-printed terahertz metalenses for next-generation communication and imaging applications. *Proc. IEEE.* **112** (8), 1033–1050 (2024).
29. Zhai, G. et al. Gain-enhanced planar log-periodic dipole array antenna using nonresonant metamaterial. *IEEE Trans. Antennas Propag.* **67** (9), 6193–6198 (2019).
30. Ge, Y., Lin, C. & Liu, Y. Broadband folded transmitarray antenna based on an ultrathin transmission polarizer. *IEEE Trans. Antennas Propag.* **66** (11), 5974–5981 (2018).
31. Pham, K. et al. Design of wideband dual linearly polarized transmit-array antennas. *IEEE Trans. Antennas Propag.* **64**(5), 2022–2026 (2016).
32. Dai, X., Wu, G. B. & Luk, K. M. A wideband low-profile reconfigureable transmitarray using magnetoelectric dipole elements, *IEEE Trans. Antennas Propag.*, vol. 70, no. 9, pp. 8008–8019, Sep. (2022).

Acknowledgements
The authors would like to thank Dassault Systemes, France, for making CST Microwave Studio available.

Author contributions
U.U and S.K did the conceptualization and wrote the main manuscript. U.U did numerical analysis. S.K did validation. A.P postprocessing and resources.All authors reviewed the manuscript.

Funding
This work was supported in part by the Icelandic Centre for Research (RANNIS) Grant 217771, and by the National Science Centre of Poland Grant 2020/37/B/ST7/01448.

Declarations

Competing interests
The authors declare no competing interests.

Additional information
Correspondence and requests for materials should be addressed to U.U.